Orientation identification of the power spectrum

EINDHOVEN UNIVERSITY OF TECHNOLOGY
Department of Mathematics and Computer Science

CASA-Report 10-71
December 2010

Orientation identification of the power spectrum

by

M.E. Rudnaya, R.M.M. Mattheij, J.M.L. Maubach

Centre for Analysis, Scientific computing and Applications
Department of Mathematics and Computer Science
Eindhoven University of Technology
P.O. Box 513
5600 MB Eindhoven, The Netherlands
ISSN: 0926-4507

Orientation identification of the power spectrum

M.E. Rudnaya, R.M.M. Mattheij , J.M.L. Maubach

CASA, Dept. of Mathematics and Computer Science, Eindhoven University of Technology

PO Box 513, 5600 MB, Eindhoven, The Netherlands

Correspondence to: M.E. Rudnaya. Tel:+31 40 247 3162; Fax:+31 40 244 2489; e-mail: m.rudnaya@tue.nl

Abstract

The image Fourier transform is widely used for defocus and astigmatism correction in electron microscopy. The shape of a power spectrum (the square of a modulus of image Fourier transform) is directly related to the three microscope's controls, namely defocus and two-fold (two-parameter) astigmatism. In this paper the new method for power spectrum orientation identification is proposed. The method is based on the three measures which are related to the microscope's controls. The measures are derived from the mathematical moments of the power spectrum. The method is tested with the help of a Gaussian benchmark, as well as with the scanning electron microscopy experimental images. The method can be used as an assisting tool for increasing the capabilities of defocus and astigmatism correction a of non-experienced scanning electron microscopy user, as well as a basis for automated application.

1 Introduction

For many practical applications in electron microscopy, both the defocus and the two-fold (two-parameter) astigmatism have to be adjusted regularly during continuous image acquiring process. Possible reasons for change in defocus and two-fold astigmatism are for instance the instabilities of the electron microscope and environment, as well as the magnetic nature of some samples. Nowadays electron microscope still requires an expert operator to trigger recording of in-focus and astigmatism-free images using a visual feedback, which is a tedious task. In future the manual operation has to be automated to improve the speed, the quality and the repeatability of the measurements.

There are different ways of automated defocus and astigmatism correction in electron microscopy. One of them is optimization of an image quality measure as a function of defocus and *two-fold* astigmatism (two-parameter astigmatism, which can be adjusted with *x-stigmator* and *y-stigmator* controls in SEM), i.e. three-parameter optimization [20, 24]. Overview of different image quality measures can be found in [11, 12, 22, 25, 30].

In general it requires more image recordings than alternative group of methods, i.e., Fourier transform-based methods.

The image Fourier transform is important for image quality improvement in electron microscopy, as well as in other types of optical devices, such as telescopes, ophthalmoscopes and endoscopes [8]. To this end, one needs on one hand a thorough analysis of the Fourier transform, on the other hand the analysis must be fast. The image's *power spectrum* - i.e., the square of a modulus of its Fourier transform - is widely used for blind deconvolution procedures [4, 28], for *defocus* and *astigmatism* correction in Scanning Electron Microscopy (SEM) [17, 18, 29], as well as in other types of electron microscopes [2, 7, 10, 26, 31, 32]. Power spectrum is used for automated defocus and astigmatism correction, as well as a visual support for a non-automated correction performed by a human operator. Unfortunately it is still hard for a non-experienced human operator to correct defocus and astigmatism within the reasonable time even with power spectrum visualization.

In this paper we discuss a new method for power spectrum orientation identification. The power spectrum model suggested in [4] is extended to a non-symmetrical case and is used for analytical derivations. Three functions corresponding to the three SEM parameters (*defocus function*, *x-stigmator function*, *y-stigmator function*) are introduced. The functions are related to the power spectrum *mathematical moments* and are chosen to simplify defocus and astigmatism correction for a non-experienced human operator. The three real-valued measures derived from the functions could be used as a basis for an automated application.

Section 2 of this paper describes the image formation model, defocus and astigmatism. Section 3 introduces power spectrum model and its discretization (Subsection 3.1). Subsection 3.2 discusses relation of a power spectrum orientation with defocus and astigmatism for the particular case of a Gaussian point spread function. Section 4 explains the method of orientation identification, which involves 1) computing defocus/stigmator functions; 2) computing defocus/stigmator measures. Subsection 4.1 discusses the particular case of power spectrum modelled as a Gaussian function. Section 5 illustrates results of numerical experiments with Gaussian benchmarks and SEM experimental images. Section 6 provides discussion and conclusions.

2 Image formation, defocus and astigmatism

According to a linear image formation model [9, 16] the microscope image is

$$f(\mathbf{u},\mathbf{p}) = (f_0(\mathbf{u}) * h(\mathbf{u},\mathbf{p}))(\mathbf{u}) := \iint_{-\infty}^{+\infty} h(\mathbf{u}',\mathbf{p}) f_0(\mathbf{u}-\mathbf{u}')\mathrm{d}\mathbf{u}'. \tag{1}$$

where $\mathbf{u} := [u,v]^T \in \mathbb{R}^2$ is a vector of *spatial coordinates*, $f_0(\mathbf{u}) \geq 0$ is the object function that describes a specimen's geometry, h is the point spread function, and $\mathbf{p} := [d,\sigma_{\mathrm{x}},\sigma_{\mathrm{y}}]^T \in \mathbb{R}^3$ is a vector of the microscope's parameters (controls), which correspond to defocus and two-fold astigmatism.

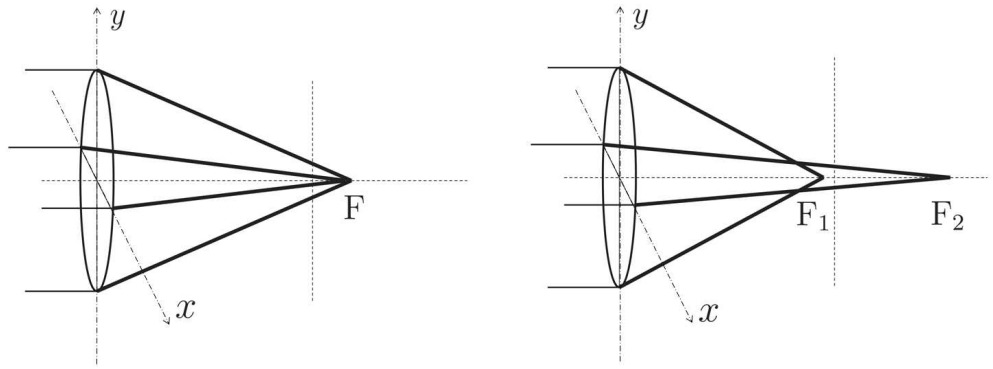

(a) (b)

Figure 1: 1(a) Ray diagram for a lens without astigmatism, the lens has one focal point; 1(b) ray diagram for a lens with astigmatism, the lens has two focal points.

Astigmatism is a lens abberation, caused by asymmetry of the lens. Figure 1(a) shows a ray diagram for the astigmatism-free situation. The lens has one focal point F. The only adjustable parameter is the current through magnetic lens; it changes the lens focal length and focuses the magnetic beam on the image plane [17]. The current is adjusted with defocus control d. Astigmatism implies that the rays traveling through a horizontal plane will be focussed at a different focal point than the rays traveling through a vertical plane (Figure 1(b)). Thus, the lens has two different focal points F_1 and F_2 and the image can not be totally sharp. Due to the presence of astigmatism, the electron beam becomes elliptic.

In SEM the point spread function can be approximated by a composition of Gaussian functions [14] or in the simplest case by one Gaussian function [5], as well as in light microscopy [15]

$$h(\mathbf{u},\mathbf{p}) = \bar{G}(\mathbf{u}) := \frac{1}{2\pi\hat{a}^2}\exp(-(\frac{u^2}{2\hat{a}^2}+\frac{v^2}{2\hat{a}^2})), \quad \hat{a}>0. \tag{2}$$

In (2) the Gaussian standard deviation (or the point spread function *width*) $\hat{a}$ is related to the defocus control d. The smaller $\hat{a}$ is the better the image f describes the object f_0. Ideally, if we assume $\hat{a}=0$, Gaussian point spread function becomes a delta function, and $f=f_0$. However, in practice the point spread function width is bounded by microscope's physical limits $\hat{a}=\hat{a}_{min}>0$. Due to the presence of astigmatism point spread function becomes elliptic

$$h(\mathbf{u},\mathbf{p}) = G(\mathbf{u}) := \frac{1}{2\pi\hat{a}\hat{b}}\exp(-(\frac{(u\cos\hat{\alpha}-v\sin\hat{\alpha})^2}{2\hat{a}^2}+\frac{(u\sin\hat{\alpha}+v\cos\hat{\alpha})^2}{2\hat{b}^2})), \tag{3}$$

$$\hat{a}>0, \quad \hat{b}>0, \quad 0\le\hat{\alpha}<\frac{\pi}{2}.$$

Figure 2(a) visualizes the roles of parameters $\hat{a},\hat{b},\hat{\alpha}$. When $\hat{a}=\hat{b}$ the value of $\hat{\alpha}$ does not play a role.

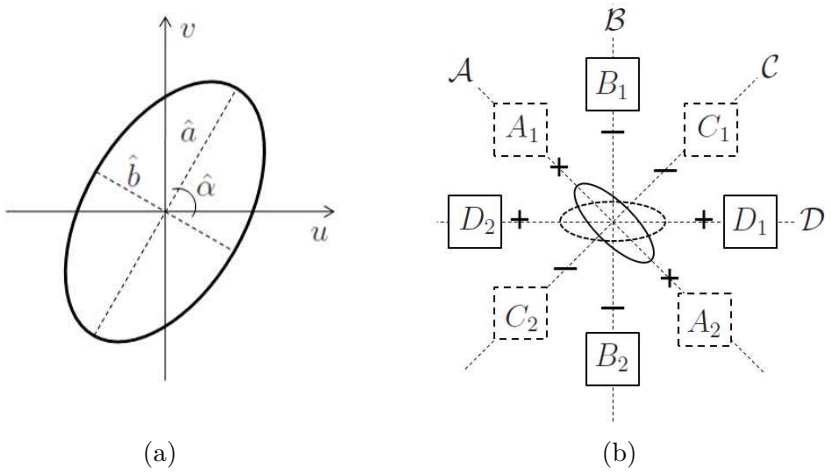

Figure 2: 2(a) Roles of parameters in elliptic function; 2(b) typical for SEM configuration of electrostatic stigmators [17].

For astigmatism correction in SEM, electrostatic or electromagnetic stigmators are used. They produce electromagnetic field for correction of the ellipticity of the electron beam [19]. A typical configuration of electrostatic stigmators for SEM is shown in Figure 2(b). The elliptic electron beam is depicted in the middle of the scheme. Currents of the same magnitude go through coils A_1, A_2, C_1, and C_2, while currents of a different magnitude go through coils B_1, B_2, D_1, and D_2. The field generated by A_1, A_2, C_1, C_2 influences the stretching of the electron beam along two orthogonal axes $\mathcal{A}$ and $\mathcal{C}$. Similarly, the field generated by coils B_1, B_2, D_1, D_2 influences the stretching along two orthogonal axes $\mathcal{C}$ and $\mathcal{D}$ [17]. The angle between axes $\mathcal{A}$ and $\mathcal{B}$ is always $\frac{\pi}{4}$. The magnitude and direction of the current through coils A_1, A_2, C_1, C_2 are controlled by the stigmator control variable σ_{x}, and the magnitude and direction of the current through coils B_1, B_2, D_1, D_2 are controlled by the stigmator control variable σ_{y}. Thus, by adjusting stigmator controls σ_{x} and σ_{y} astigmatism is corrected.

For defocus and astigmatism correction problem, we consider a vector of three microscope's control variables $\mathbf{p} := [d, \sigma_{\mathrm{x}}, \sigma_{\mathrm{y}}]^T$ with the ideal parameter values (the ideal parameter values correspond to the image of the highest possible quality) denoted as $\mathbf{p}_0 := [d_0, \sigma_{\mathrm{x}_0}, \sigma_{\mathrm{y}_0}]^T$.

3 Power spectrum theory

For the vector of *frequency coordinates* $\mathbf{x} := [x, y]^T$, an image $f(\mathbf{u})$, its power spectrum $p(\mathbf{x})$ is a square of a modulus of the image's Fourier transform

$$p(\mathbf{x}) := |\mathfrak{F}[f]|^2.$$

The image f is real-valued. Hence, one finds

$$p(\mathbf{x}) = p(-\mathbf{x}). \tag{4}$$

In Fourier space convolution becomes multiplication, thus (1) can be rewritten as

$$\mathfrak{F}[f] = \mathfrak{F}[f_0]\mathfrak{F}[h]$$

or

$$p(\mathbf{x}) = |\mathfrak{F}[f_0]|^2 |\mathfrak{F}[h]|^2. \tag{5}$$

According to [3, 4] a rotationally symmetric power spectrum can be modelled as a function

$$p(\mathbf{x}) = \bar{g}(\mathbf{x}) := A \exp(-(\frac{x^2}{2a^2} + \frac{y^2}{2a^2})^\beta), \quad 0 < \beta \leq 1, \quad a > 0, \quad A > 0. \tag{6}$$

This is a consequence of the fact that in a variety of optical systems point spread function h can be often approximated by a *Lévy stable density* with parameter β, which is a property of an optical device (in our case, SEM). For $\beta = 1$ one obtains the Gaussian function and for $\beta = \frac{1}{2}$ - *Lorentzian (or Cauchy) function*. When $\beta = 1$, h has slim tails and finite variance. When $0 < \beta < 1$, h has fat tails and infinite variance [4].

Due to the presence of astigmatism power spectrum might loose its rotational symmetry. Therefore we extend (6) to a non-symmetric case

$$p(\mathbf{x}) = g(\mathbf{x}) := A \exp(-(\frac{(x\cos\alpha - y\sin\alpha)^2}{2a^2} + \frac{(x\sin\alpha + y\cos\alpha)^2}{2b^2})^\beta), \tag{7}$$

$$a > 0, \quad b > 0, \quad 0 \leq \alpha < \frac{\pi}{2}.$$

For polar coordinates

$$\mathbf{r} := [r, \varphi]^T \in \{\mathbb{R}^+ \times [0, 2\pi)\}, \quad x = r\cos\varphi, \quad y = r\sin\varphi,$$

it becomes

$$g(\mathbf{x}) = A \exp(-r^{2\beta}(\frac{\cos^2(\varphi + \alpha)}{2a^2} + \frac{\sin^2(\varphi + \alpha)}{2b^2})^\beta). \tag{8}$$

3.1 Discretization

We assume that the continuous power spectrum $p(\mathbf{x})$ has a compact support inside

$$\mathbb{X} := [-X, X] \times [-X, X],$$

which means

$$p(\mathbf{x}) = 0, \quad \forall \mathbf{x} \notin \mathbb{X}.$$

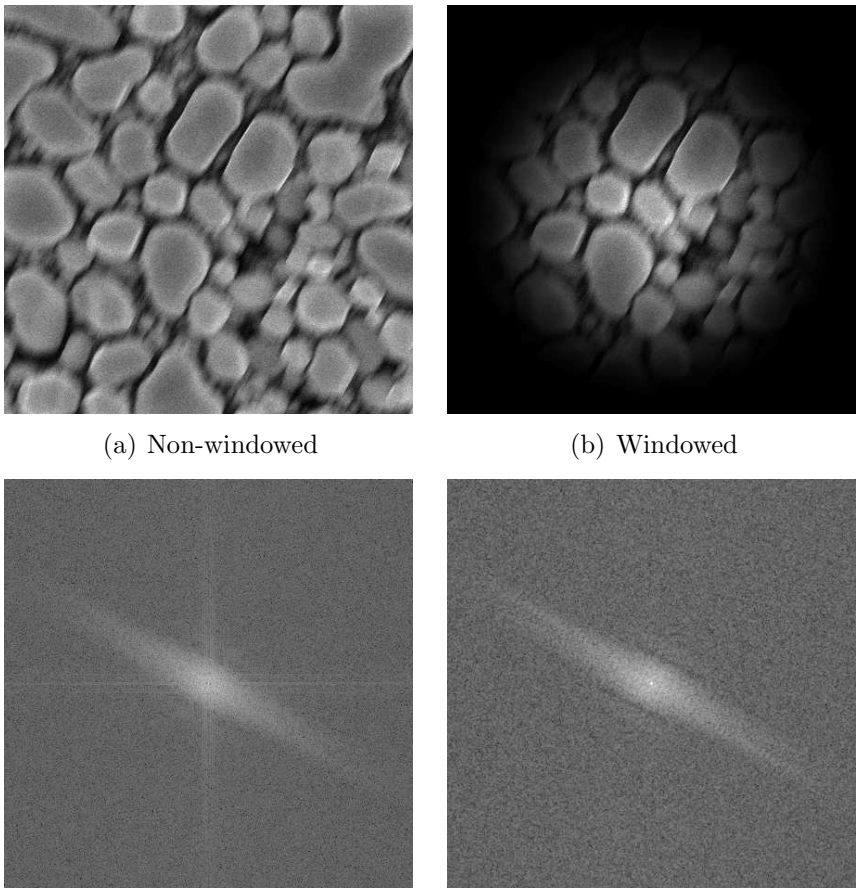

(a) Non-windowed (b) Windowed

(c) power spectrum non-windowed (d) power spectrum windowed

Figure 3: 3(a) A SEM experimental image of Gold-on-Carbon (a non-windowed image); 3(b) the experimental image multiplied by the window function (a windowed image); 3(c) power spectrum of the experimental non-windowed image; 3(d) power spectrum of the experimental windowed image.

In practice images are always discrete and can be represented by matrixes

$$\mathbf{F} \in \mathbb{R}^{(2n+1)\times(2n+1)}, \quad n \in \mathbb{N}.$$

A corresponding discrete power spectrum $\mathbf{P} := (P_{i,j})_{i,j=1}^{2n+1}$ can be computed with the *Fast Fourier Transform* method [6, 13].

We define frequency mesh points $x_i := i\Delta x, \quad y_j := j\Delta x, \quad i, j = -n, \ldots, n$, where

$$\Delta x := \frac{2X}{(2n+1)-1} = \frac{X}{n}. \tag{9}$$

Then we define

$$P_{i,j} := p(x_i, y_j). \tag{10}$$

The power spectrum $\mathbf{P}$ has a high dynamic range: low frequencies (pixels with indices close to $(i, j) = (0, 0)$) have much higher values than high frequencies. A normal output graphic device does not have a sufficient dynamic range to display it simultaneously. It is suggested to use logarithmic scale for power spectrum vizualization [9]

$$P_{i,j}^{(C)} = \log(C + P_{i,j}), \tag{11}$$

where C is a scaling constant for the contrast adjustments. In this paper, as well as in [4], we use $C = 0$ for power spectrum visualization.

Fast Fourier Transform method is based on the assumption of function periodicity [13], which is usually not the case for the real-world images. Before the discrete power spectrum computations it is important to multiply the image by a *Window function*, for instance with

$$W(\mathbf{x}, x_{max}) := \begin{cases} (1 + \cos(\frac{\pi|\mathbf{x}|}{x_{max}}))/2, \text{ if } |\mathbf{x}| \le x_{max}, \\ 0, \text{ elsewise}, \end{cases} \tag{12}$$

in order to avoid discontinuities on the boundary. For the discrete image we make a choice of $x_{max} = x_{n-1}$. Figure 3 shows the difference between power spectrums of the non-windowed image and the windowed image. The non-windowed power spectrum (Figure 3(c)) has two orthogonal lines crossing in the origin, while the windowed power spectrum (Figure 3(d)) shows only elliptic distribution. The lines in the non-widowed power spectrum (Figure 3(c)) are results of discontinuity and can result in the errors during the further power spectrum analysis.

3.2 Power spectrum orientation in relation to defocus and astigmatism

The power spectrum of a Gaussian point spread function (3) is a Gaussian function

$$|\mathfrak{F}[G]|^2 = \hat{A} \exp(-(\hat{a}^2(x\cos\hat{\alpha} - y\sin\hat{\alpha})^2 + \hat{b}^2(x\sin\hat{\alpha} + y\cos\hat{\alpha})^2)), \tag{13}$$

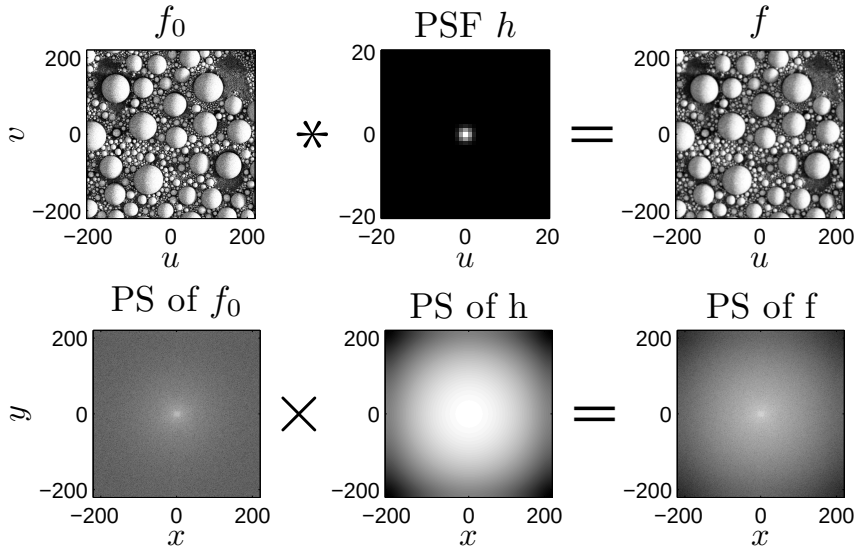

Figure 4: The upper row represents real space (spatial coordinates $\mathbf{u} := [u, v]^T$); from left to right: Experimental SEM image, which is considered to be the object function f_0, Gaussian point spread function h ($\hat{a} = \hat{b} = 1, \hat{\alpha} = 0$), numerical result of their convolution f. The lower row represents the three mentioned quantities in the Fourier space (frequency coordinates $\mathbf{x} := [x, y]^T$). PS denotes the Power Spectrum. PSF denotes the point spread function.

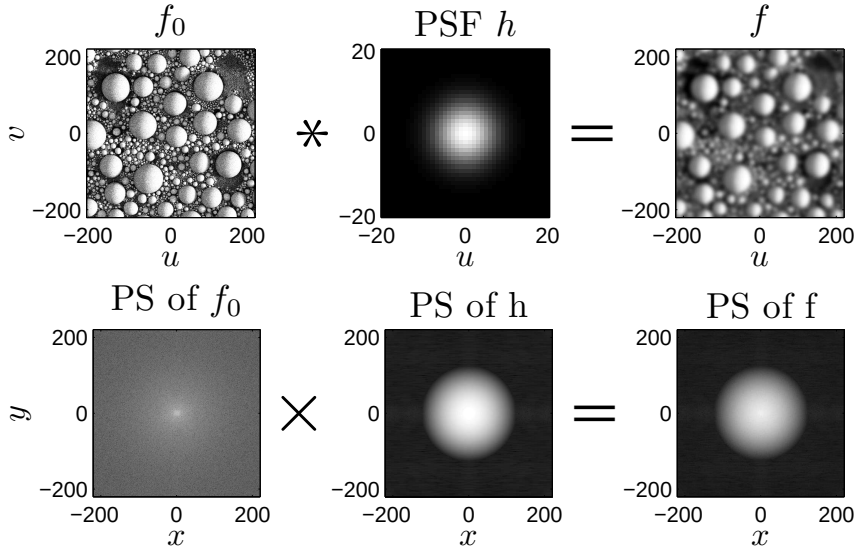

Figure 5: Similar to Figure 4 numerical computation, but with the Gaussian point spread function parameters $\hat{a} = \hat{b} = 5, \hat{\alpha} = 0$. PS denotes the Power Spectrum. PSF denotes the point spread function.

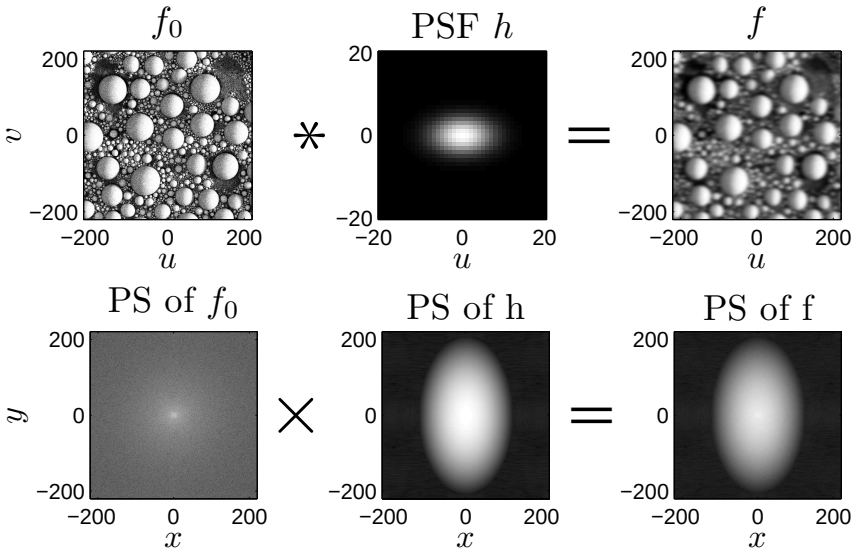

Figure 6: Similar to Figure 4 numerical computation, but with the Gaussian point spread function parameters $\hat{a} = 5, \hat{b} = 3, \hat{\alpha} = 0$. PS denotes the Power Spectrum. PSF denotes the point spread function.

where $\hat{A} > 0$ is a constant. The rotation angle of the Gaussian power spectrum is equal to the rotational angle in real space, and the widths are inversely proportional to the width in real space.

We illustrate relation of power spectrum orientation to defocus and astigmatism with the help of three numerical examples. Left columns of figures 4-6 show the same experimental image of tin balls obtained with SEM and its power spectrum. For numerical experiment we consider this image to be an ideal image, i.e. the object function of a specimen f_0. The power spectrum is nearly rotationally symmetric. The image is convolved sequentially with a Gaussian point spread functions with parameters $\hat{a} = \hat{b} = 1, \hat{\alpha} = 0$ (Figure 4), $\hat{a} = \hat{b} = 5, \hat{\alpha} = 0$ (Figure 5), $\hat{a} = 5, \hat{b} = 3, \hat{\alpha} = 0$ (Figure 6). The upper row of each figure represents real space, and the low row represents Fourier space, where convolution becomes multiplication. The influence of the point spread function's parameters is visible in the result of the convolution in real space (image f - the top right of each of the figures), as well as in the Fourier space.

When consider a rotationally symmetric point spread function with a relatively small width (Figure 4) the final image f does not deviate a lot from original f_0. Its power spectrum is rotationally symmetric and has, as well as the power spectrum of the point spread function, relatively large width. When consider a rotationally symmetric point spread function with a larger width (Figure 5), its power spectrum has a smaller width, as well as the power spectrum of f (power spectrum's intensity decreases), and the image f itself looks more blurred than in Figure 4. Further, when consider a non-symmetric point spread function, the power spectrum of f becomes non-symmetric as well (Figure 6).

The knowledge of the described above power spectrum behavior is used by a human

operator during the defocus and astigmatism correction, when adjusting the controls $\mathbf{p}$. For the amorphous object with rotationally symmetric power spectrum, operator tries to obtain an image with power spectrum as intense as possible without stretching in any direction. The difficult situation is when the power spectrum of the object f_0 is not rotationally symmetric (the object has a strong preferential direction). In this case it is important to compare the difference between power spectrums obtained for different $\mathbf{p}$ and to find a center of symmetry [17].

It is often difficult for a non-experienced human operator to understand, which of the controls $\mathbf{p}$ and in which directions are to be adjusted just from observing elliptic power spectrum. In the next section we provide a methodology to simplify the correction for a human. Also, this methodology can be used as a basis for automated defocus and astigmatism correction method.

4 Orientation identification method

With the power spectrum $p(\mathbf{x}) = p(r\cos\varphi, r\sin\varphi)$, we associate the three functions

$$\mathrm{h}_0(r) := \oint_0^{2\pi} p(r\cos\varphi, r\sin\varphi)\mathrm{d}\varphi, \tag{14}$$

$$\mathrm{h}_1(r) := \oint_0^{2\pi} p(r\cos\varphi, r\sin\varphi)\cos 2\varphi\mathrm{d}\varphi, \tag{15}$$

$$\mathrm{h}_2(r) := \oint_0^{2\pi} p(r\cos\varphi, r\sin\varphi)\sin 2\varphi\mathrm{d}\varphi. \tag{16}$$

The function h_0 (*defocus function*) is related to the defocus d. It is clear that $\mathrm{h}_0(r) \geq 0$ ($p(\mathbf{x}) \geq 0$ by definition). The functions h_1 (*x-stigmator function*) and h_2 (*y-stigmator function*) are related to the stigmators σ_x, σ_y respectively. In (15) and (16) $\cos 2\varphi$ and $\sin 2\varphi$ play the roles of the weight functions. Below it will be shown for particular examples how they help to obtain information about the signs of the stigmators σ_x and σ_y. Due to the power spectrum symmetry (4)

$$\mathrm{h}_0(r) = 2\oint_0^{\pi} p(r\cos\varphi, r\sin\varphi)\mathrm{d}\varphi, \tag{17}$$

$$\mathrm{h}_1(r) = 2\oint_0^{\pi} p(r\cos\varphi, r\sin\varphi)\cos 2\varphi\mathrm{d}\varphi, \tag{18}$$

$$\mathrm{h}_2(r) = 2\oint_0^{\pi} p(r\cos\varphi, r\sin\varphi)\sin 2\varphi\mathrm{d}\varphi. \tag{19}$$

The representation (17)-(19) makes further numerical computations faster.

The defocus and stigmator functions (14)-(16) are related to the mathematical moments of the power spectrum

$$m_{k,l} := \iint_{-\infty}^{+\infty} x^k y^l p(\mathbf{x})\mathrm{d}\mathbf{x} = \int_0^{\infty} r^{k+l+1}\oint_0^{2\pi} p(r\cos\varphi, r\sin\varphi)\cos^k\varphi\sin^l\varphi\mathrm{d}\varphi\mathrm{d}r,$$

which are widely used in different applications for orientation identification and other purposes [27, 33, 34]. The 0-moment is

$$m_{0,0} = \int_0^\infty r\mathrm{h}_0(r)\mathrm{d}r. \tag{20}$$

The symmetry of the power spectrum (4) leads to the fact the 1st moments are equal to zero

$$m_{1,0} = \int_0^\infty r^2 \oint_0^{2\pi} p(r\cos\varphi, r\sin\varphi)\cos\varphi \mathrm{d}\varphi\mathrm{d}r = 0,$$
$$m_{0,1} = \int_0^\infty r^2 \oint_0^{2\pi} p(r\cos\varphi, r\sin\varphi)\sin\varphi \mathrm{d}\varphi\mathrm{d}r = 0.$$

The 2nd moments are:

$$m_{2,0} = \int_0^\infty r^3 \oint_0^{2\pi} p(r\cos\varphi, r\sin\varphi)\cos^2\varphi \mathrm{d}\varphi\mathrm{d}r \underset{\cos^2\varphi=\frac{1}{2}+\frac{1}{2}\cos 2\varphi}{=} \frac{1}{2}\int_0^\infty r^3(\mathrm{h}_0(r)+\mathrm{h}_1(r))\mathrm{d}r, \tag{21}$$

$$m_{0,2} = \int_0^\infty r^3 \oint_0^{2\pi} p(r\cos\varphi, r\sin\varphi)\sin^2\varphi \mathrm{d}\varphi\mathrm{d}r \underset{\sin^2\varphi=\frac{1}{2}-\frac{1}{2}\cos 2\varphi}{=} \frac{1}{2}\int_0^\infty r^3(\mathrm{h}_0(r)-\mathrm{h}_1(r))\mathrm{d}r, \tag{22}$$

$$m_{1,1} = \int_0^\infty r^3 \oint_0^{2\pi} p(r\cos\varphi, r\sin\varphi)\cos\varphi\sin\varphi \mathrm{d}\varphi\mathrm{d}r = \frac{1}{2}\int_0^\infty r^3\mathrm{h}_2(r)\mathrm{d}\varphi\mathrm{d}r. \tag{23}$$

Based on (21)-(23) we introduce the three measures

$$s_q := \int_0^\infty r^3\mathrm{h}_q(r)\mathrm{d}r, \quad q = 0, 1, 2, \tag{24}$$

related to the second mathematical moments as follows from (22)-(23)

$$m_{2,0} = \frac{1}{2}(s_0 + s_1),$$

$$m_{0,2} = \frac{1}{2}(s_0 - s_1),$$

$$m_{1,1} = \frac{1}{2}s_2.$$

For the particular case of the function (8), it follows that

$$s_0 = A\pi ab\Gamma(1+\frac{2}{\beta})(b^2+a^2), \tag{25}$$

$$s_1 = A\pi ab\Gamma(1+\frac{2}{\beta})(b^2-a^2)\cos 2\alpha, \tag{26}$$

$$s_2 = A\pi ab\Gamma(1+\frac{2}{\beta})(b^2-a^2)\sin 2\alpha, \tag{27}$$

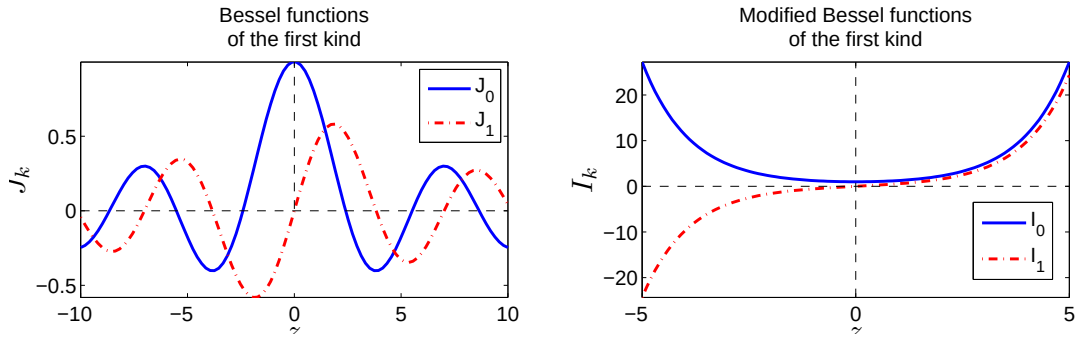

Figure 7: Bessel functions of the first kind and modified Bessel functions of the first kind for $k = 0, 1$.

where Γ is the Gamma function

$$\Gamma(z) := \int_0^{+\infty} t^{z-1} e^{-t} \mathrm{d}t, \quad z > 0.$$

For the particular case of a Gaussian function $\Gamma(3) = 2$. Consider the power spectrum function (8). Then parameter α can be directly estimated from numerically computed values of s_1 and s_2

$$\alpha = \begin{cases} \frac{1}{2}\arctan(\frac{s_2}{s_1}), & \text{if } s_1 \neq 0, \\ \frac{\pi}{4}, & \text{if } s_1 = 0, \quad s_2 \neq 0, \\ \forall, & \text{if } s_1 = 0, \quad s_2 = 0. \end{cases} \tag{28}$$

4.1 Gaussian power spectrum

Consider the power spectrum modelled as a Gaussian function ($\beta = 1$ in (7)). Then one can rewrite the expressions for defocus and stigmator functions (14) - (16) as follows

$$\mathrm{h}_0(r) = \oint_0^{2\pi} e^{-r^2(\frac{\cos^2(\varphi+\alpha)}{2a^2}+\frac{\sin^2(\varphi+\alpha)}{2b^2})} \mathrm{d}\varphi = 2e^{-\frac{(a^2+b^2)r^2}{4a^2b^2}} \pi I_0(\frac{1}{4}(\frac{1}{b^2} - \frac{1}{a^2})r^2),$$

$$\mathrm{h}_1(r) = \oint_0^{2\pi} e^{-r^2(\frac{\cos^2(\varphi+\alpha)}{2a^2}+\frac{\sin^2(\varphi+\alpha)}{2b^2})} \cos 2\varphi \mathrm{d}\varphi = 2e^{-\frac{(a^2+b^2)r^2}{4a^2b^2}} \pi I_1(\frac{1}{4}(\frac{1}{b^2} - \frac{1}{a^2})r^2) \cos 2\alpha,$$

$$\mathrm{h}_2(r) = \oint_0^{2\pi} e^{-r^2(\frac{\cos^2(\varphi+\alpha)}{2a^2}+\frac{\sin^2(\varphi+\alpha)}{2b^2})} \sin 2\varphi \mathrm{d}\varphi = 2e^{-\frac{(a^2+b^2)r^2}{4a^2b^2}} \pi I_1(\frac{1}{4}(\frac{1}{b^2} - \frac{1}{a^2})r^2) \sin 2\alpha,$$

where $I_k(z)$ is the *Modified Bessel Function of the first kind*, that can be expressed as [1]

$$I_k(z) := \frac{1}{\pi} \int_0^{\pi} e^{r\cos\varphi} \cos k\varphi \mathrm{d}\varphi,$$

which is related to the *Bessel Function of the first kind* as [1]

$$I_k(z) := \mathrm{i}^{-k} J_k(\mathrm{i}z).$$

Figure 7 shows Bessel functions of the first kind and modified Bessel functions of the first kind for $k = 0, 1$.

From these observations it is clear for the particular case of a Gaussian function that

$$\begin{cases} \mathrm{h}_1 < 0, \text{ if } a < b \text{ and } \alpha \neq \frac{\pi}{4}, \\ \mathrm{h}_1 = 0, \text{ if } a = b \text{ or } \alpha = \frac{\pi}{4}, \\ \mathrm{h}_1 > 0, \text{ if } a > b \text{ and } \alpha \neq \frac{\pi}{4}. \end{cases} \tag{29}$$

and

$$\begin{cases} \mathrm{h}_2 < 0, \text{ if } a < b \text{ and } \alpha \neq 0, \\ \mathrm{h}_2 = 0, \text{ if } a = b \text{ or } \alpha = 0, \\ \mathrm{h}_2 > 0, \text{ if } a > b \text{ and } \alpha \neq 0. \end{cases} \tag{30}$$

It means that the directions of stigmator controls variables can be easily identified from the stigmator functions

$$\begin{cases} \sigma_{\mathrm{x}} < \sigma_{\mathrm{x}_0}, \text{ if } \mathrm{h}_1 < 0, \\ \sigma_{\mathrm{x}} = \sigma_{\mathrm{x}_0}, \text{ if } \mathrm{h}_1 = 0, \\ \sigma_{\mathrm{x}} > \sigma_{\mathrm{x}_0}, \text{ if } \mathrm{h}_1 > 0, \end{cases} \tag{31}$$

and

$$\begin{cases} \sigma_{\mathrm{y}} < \sigma_{\mathrm{y}_0}, \text{ if } \mathrm{h}_2 < 0, \\ \sigma_{\mathrm{y}} = \sigma_{\mathrm{y}_0}, \text{ if } \mathrm{h}_2 = 0, \\ \sigma_{\mathrm{y}} > \sigma_{\mathrm{y}_0}, \text{ if } \mathrm{h}_2 > 0. \end{cases} \tag{32}$$

4.2 Discretization

We define the radial mesh points $r_k = k\Delta r + \frac{\Delta r}{2}, k = 1, \ldots, N$, where $\Delta r := \frac{X}{N}$, and the angular mesh points $\varphi_l = l\Delta\varphi + \frac{\Delta\varphi}{2}, l = 1, \ldots, M$, where $\Delta\varphi := \frac{\pi}{M}$. Further we fill in the matrix values $\tilde{\mathbf{P}} \in \mathbb{R}^{N\times M}$

$$x^{(k,l)} := r_k \cos\varphi_l, \quad y^{(k,l)} := r_k \sin\varphi_l. \tag{33}$$

Each point $(x^{(k,l)}, y^{(k,l)})$ is bounded

$$x_{i-1} \leq x^{(k,l)} \leq x_i, \quad y_{j-1} \leq y^{(k,l)} \leq y_j, \quad i \in \{-n+1, \ldots, n\}, \quad j \in \{-n+1, \ldots, n\}.$$

We compute values of $\tilde{\mathbf{P}}_{k,l}$ with a linear interpolation (see Figure 8)

$$\tilde{\mathbf{P}}_{k,l} = ((1 - \frac{\delta_x}{\Delta x})p_{i-1,j-1} + \frac{\delta_x}{\Delta x}p_{i,j-1})(1 - \frac{\delta_y}{\Delta x}) + ((1 - \frac{\delta_x}{\Delta x})p_{i-1,j} + \frac{\delta_x}{\Delta x}p_{i,j})\frac{\delta_y}{\Delta x},$$

where

$$\delta_x := x^{(k,l)} - x_{i-1}, \quad \delta_y := y^{(k,l)} - y_{i-1}.$$

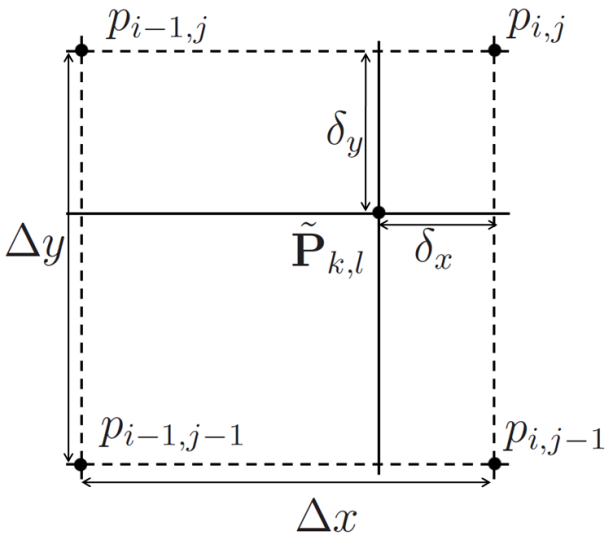

Figure 8: Linear interpolation of power spectrum values.

For $k \in \{1, \ldots, N\}$ we approximate the values of $\mathrm{h}_0(r_k), \mathrm{h}_1(r_k), \mathrm{h}_2(r_k)$ with the midpoint numerical integration rule

$$\mathrm{h}_0(r_k) \doteq 2\Delta\varphi \sum_{l=1}^{M} \tilde{\mathbf{P}}_{k,l}, \tag{34}$$

$$\mathrm{h}_1(r_k) \doteq 2\Delta\varphi \sum_{l=1}^{M} \tilde{\mathbf{P}}_{k,l} \cos 2\varphi_l, \tag{35}$$

$$\mathrm{h}_2(r_k) \doteq 2\Delta\varphi \sum_{l=1}^{M} \tilde{\mathbf{P}}_{k,l} \sin 2\varphi_l. \tag{36}$$

Then the measures are approximated with the midpoint rule too

$$s_q \doteq \Delta r \sum_{k=1}^{N} r_k^3 \mathrm{h}_q(r_k), \quad q = 1, 2, 3. \tag{37}$$

5 Numerical experiments

5.1 Numerical experiments for a Gaussian function

We consider a discrete Gaussian function with dimensions $(2n+1) \times (2n+1) = 101 \times 101$ pixels. For further numerical computations of defocus and stigmator functions $\mathrm{h}_0, \mathrm{h}_1, \mathrm{h}_2$, the number of data points for discretization of polar radius r is chosen $N = n = 50$ and for discretization of polar angle φ is chosen $M = 2(2n+1) = 202$. We consider $\Delta x = 1$ in (9),

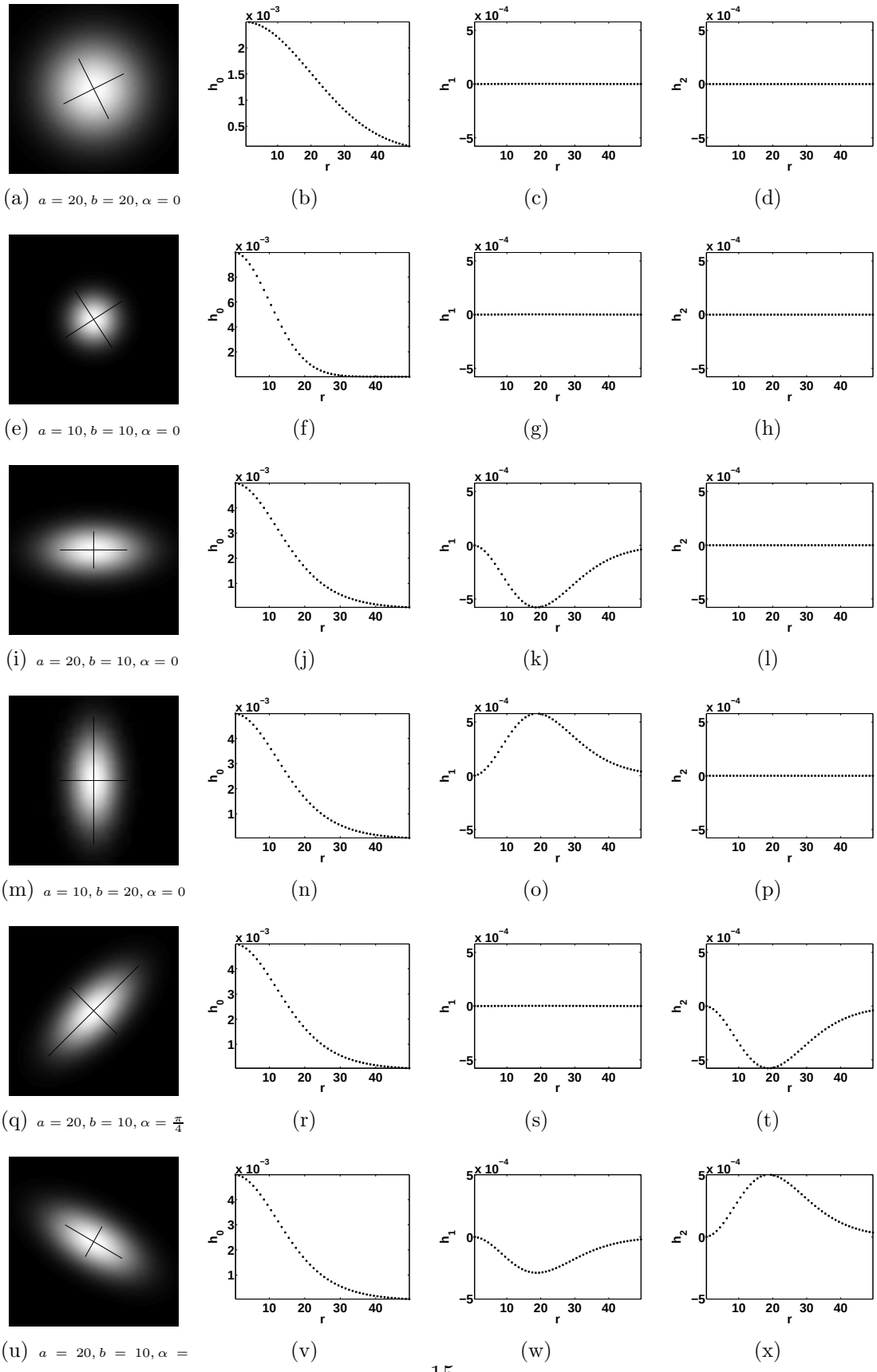

(a) $a = 20, b = 20, \alpha = 0$ (b) (c) (d)

(e) $a = 10, b = 10, \alpha = 0$ (f) (g) (h)

(i) $a = 20, b = 10, \alpha = 0$ (j) (k) (l)

(m) $a = 10, b = 20, \alpha = 0$ (n) (o) (p)

(q) $a = 20, b = 10, \alpha = \frac{\pi}{4}$ (r) (s) (t)

(u) $a = 20, b = 10, \alpha = -\frac{\pi}{6}$ (v) (w) (x)

Figure 9: Numerical computations for a Gaussian benchmark.

thus $X = n$. Each row of Figure 9 shows a Gaussian functions with particular parameters values a, b, α and corresponding $\mathrm{h}_0, \mathrm{h}_1, \mathrm{h}_2$ functions. The rotation angle α is numerically estimated according to (28) and indicated by two orthogonal lines plotted above each of the Gaussian functions.

Below we provide an overview of illustrated numerical experiments:

1. Figures 9(a)-9(d): Gaussian is rotationally symmetric ($a = b = 20$). For this reason the computed values of h_1 and h_2 are equal to zero.

2. Figures 9(e)-9(h): Gaussian is rotationally symmetric ($a = b = 10$). The values of h_1 and h_2 are equal to zero. The value of Gaussian width is smaller than in Figures 9(a). The integral of the function h_0 in Figure 9(f) decreases in comparison with the previous experiment (Figure 9(b)). The goal of a human operator in this case is to find the SEM parameters such that the Gaussian width and as a consequence the integral of h_0 is as large as possible. In order to estimate h_0 intensity and to minimize the defocus in automated applications the measure based on the zero mathematical moment (20) is often used in electron microscopy [21, 22]

$$s_{0,0} := \int_{r_{min}}^{r_{max}} r \int_0^{2\pi} p(r\cos\varphi, r\sin\varphi)\mathrm{d}\varphi\mathrm{d}r,$$

   where r_{min} and r_{max} are the low frequency band and high frequency band, parameters given as an input by a user.

3. Figures 9(i)-9(l): Elliptic Gaussian. The widths $a > b$ and as a consequence all the values of h_1 are smaller than zero. The values of h_2 are equal to zero, because $\alpha = 0$.

4. Figures 9(m)-9(p): Elliptic Gaussian. The widths $b > a$ and as a consequence all the values of h_1 are larger than zero. The values of h_2 are equal to zero, because $\alpha = 0$.

5. Figures 9(q)-9(t): Elliptic Gaussian with $a > b, \alpha = \frac{\pi}{4}$. As a consequence $\mathrm{h}_1 = 0, \mathrm{h}_2 < 0$.

6. Figures 9(u)-9(x): Elliptic Gaussian with $a > b, \alpha = -\frac{\pi}{6}$. As a consequence $\mathrm{h}_1 < 0, \mathrm{h}_2 > 0$.

The numerical results correspond to the analytical observations (29)-(30) and can guide an unexperienced human operator, giving visual suggestion about a proper choice of stigmator control and its sign (31)-(32).

5.2 Numerical experiments for SEM images

In this section the functions $\mathrm{h}_0, \mathrm{h}_1, \mathrm{h}_2$ are computed for power spectrums of SEM experimental images. The rotation angle α is numerically estimated using (28). Each of the figures 10-14 show

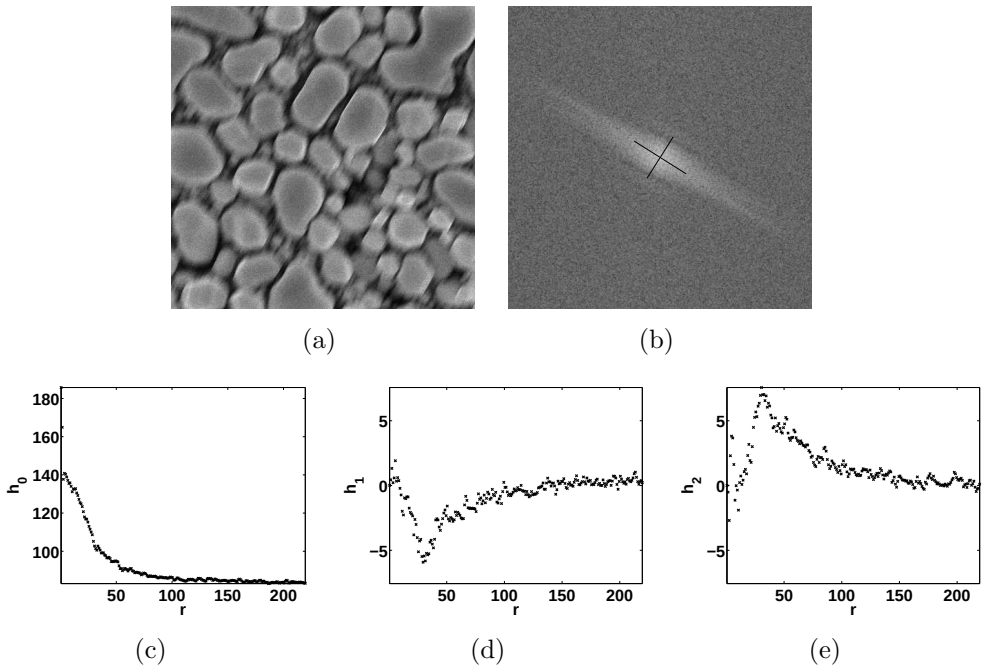

Figure 10: From left to right, from top to bottom: SEM experimental image, logarithmic scale of its power spectrum, numerically computed functions $\mathrm{h}_0(r), \mathrm{h}_1(r), \mathrm{h}_2(r)$.

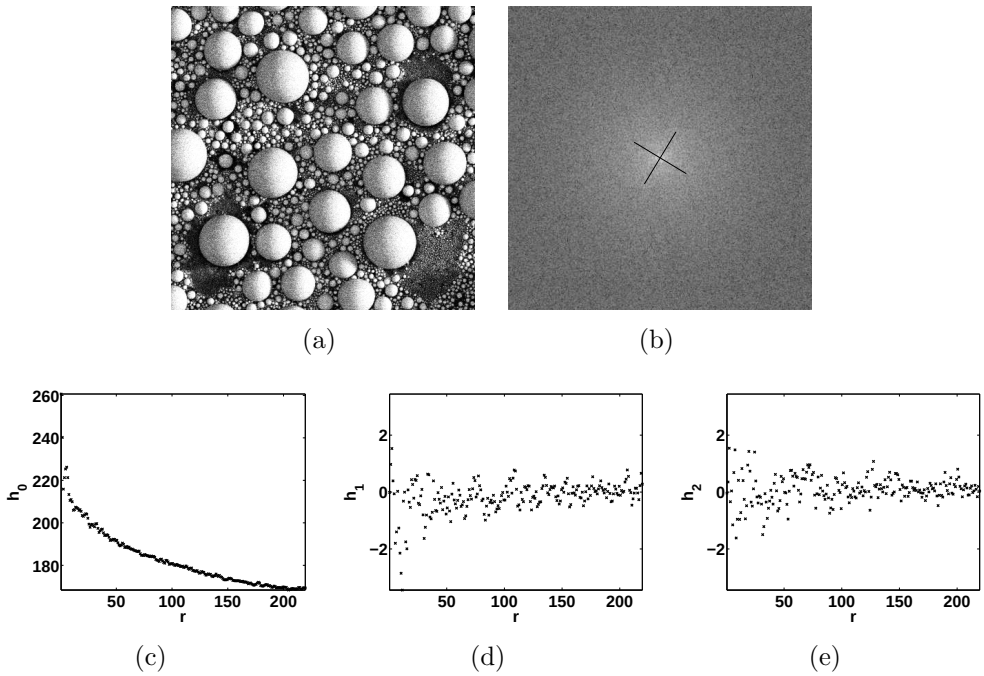

Figure 11: From left to right, from top to bottom: SEM experimental image, logarithmic scale of its power spectrum, numerically computed functions $\mathrm{h}_0(r), \mathrm{h}_1(r), \mathrm{h}_2(r)$.

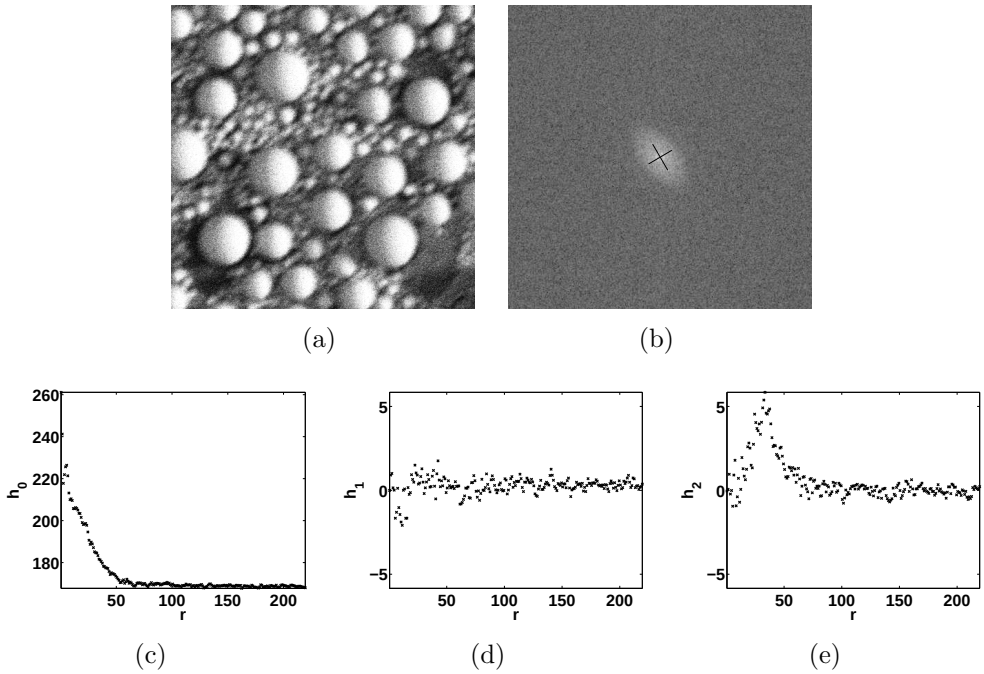

Figure 12: From left to right, from top to bottom: SEM experimental image, logarithmic scale of its power spectrum, numerically computed functions $\mathrm{h}_0(r), \mathrm{h}_1(r), \mathrm{h}_2(r)$.

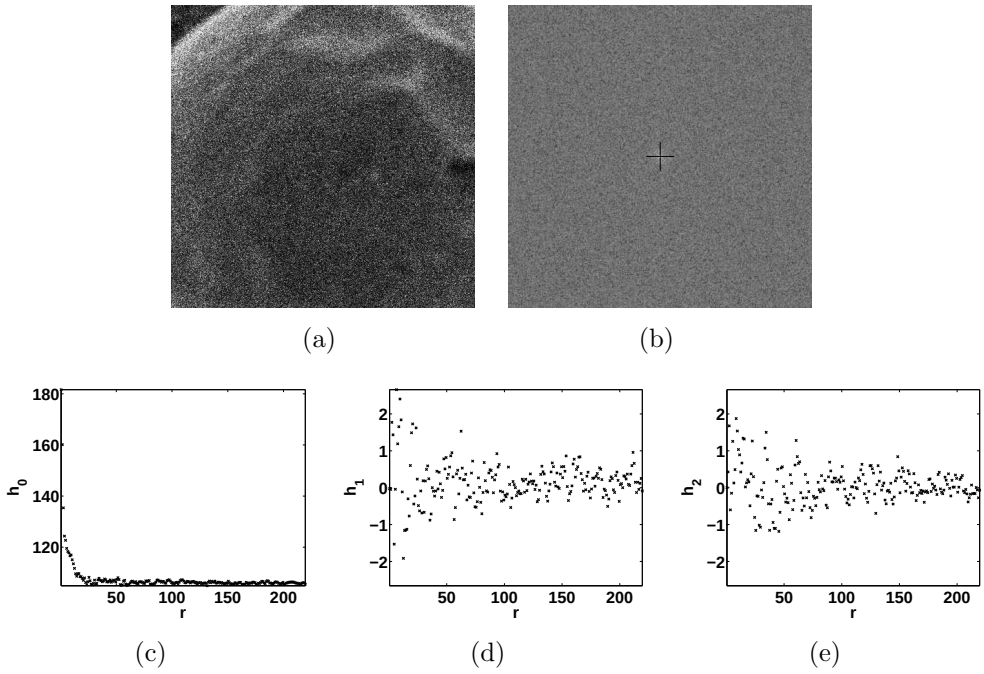

Figure 13: From left to right, from top to bottom: SEM experimental image, logarithmic scale of its power spectrum, numerically computed functions $\mathrm{h}_0(r), \mathrm{h}_1(r), \mathrm{h}_2(r)$.

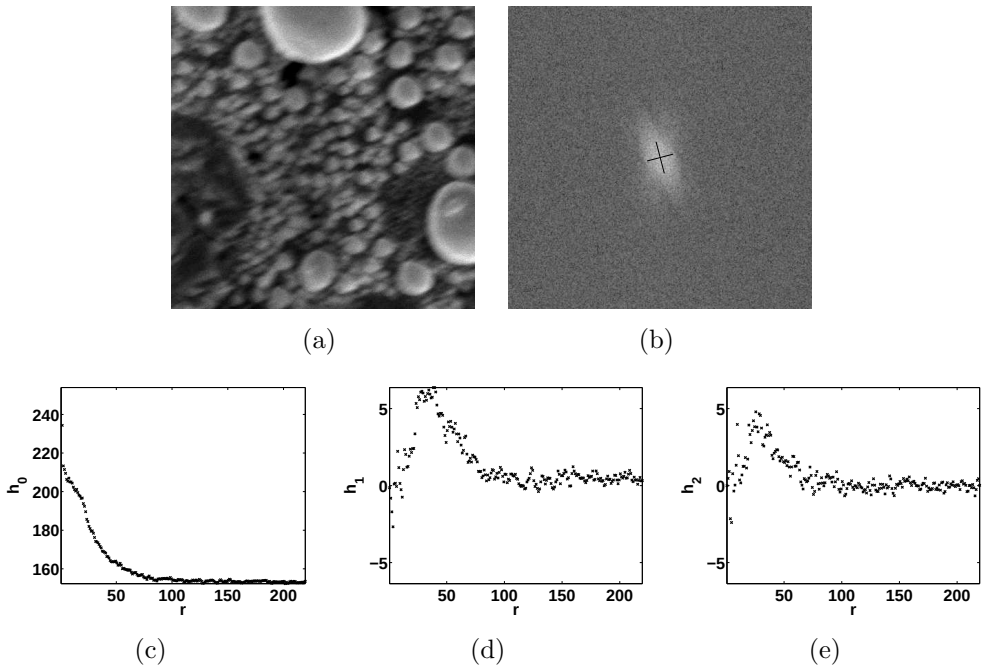

Figure 14: From left to right, from top to bottom: SEM experimental image, logarithmic scale of its power spectrum, numerically computed functions $\mathrm{h}_0(r), \mathrm{h}_1(r), \mathrm{h}_2(r)$.

- SEM experimental image;
- Logarithmic scale of its power spectrum;
- Functions $\mathrm{h}_0, \mathrm{h}_1, \mathrm{h}_2$ computed with (34)-(36).

The size of each experimental image is $(2n+1) \times (2n+1) = 441 \times 441$ pixels. For each function $\mathrm{h}_0, \mathrm{h}_1, \mathrm{h}_2$ the measures s_0, s_1, s_2 are computed with (37), and the following values chosen $\Delta x = 1, N = n = 220, M = 2(2n+1) = 882$. Further, the angle α is identified using (28). Two orthogonal lines above each power spectrum visualize the observed value of α. The functions $\mathrm{h}_0, \mathrm{h}_1, \mathrm{h}_2$ shown in the figures are computed for the logarithmic scale of power spectrum for the reason of convenience of visualization. However, the angle α displayed by the two orthogonal lines is found from defocus and stigmator functions before the logarithmic scale.

Figure 10 shows the experiment for Gold-on-Carbon stigmatic image. Changing both σ_{x} and σ_{y} is needed to improve the quality. The signs of the curves h_1 and h_2 indicate the direction of change. Figure 11 shows in-focus astigmatism-free image of tin balls. Both h_1 and h_2 are numerical noise around zero. Figure 12 shows defocused stigmatic image of the same sample. We can see how the image quality decreases and power spectrum shape changes. The y-stigmator function suggests the change of σ_{y}, while adjustment of σ_{x} does not seem to be necessary. Figure 13 shows a magnified image of tin balls. The image does not have a lot of details and as a consequence its power spectrum has only a

few values of low frequencies different from noise. Because of the lack of information in Fourier space of the image, it is difficult to analyse this power spectrum and to draw the conclusions about the presence of astigmatism in the image. In the case of this type of samples the method of orientation identification as well as other Fourier transform-based methods might fail. Figure 14 shows one more defocused and stigmatic image. We can clearly see that correction of both σ_{x} and σ_{y} is needed.

6 Discussion and conclusions

The method for power spectrum orientation identification was proposed and tested on Gaussian benchmarks and on SEM experimental images. The method involves computing of defocus/stigmator functions and defocus/stigmator real-valued measures. For power spectrum modelled as a Lévy stable density, the defocus/stigmator measures are expressed via the Gamma function. For power spectrum modelled as a Gaussian function (the particular case of a Lévy stable density), the defocus/stigmator functions are expressed via the Modified Bessel functions of the first kind. The method can be used for increasing the capabilities of defocus and astigmatism correction for non-experienced SEM users (via defocus/stigmator functions). The method could be used as a basis for automated defocus and astigmatism correction in SEM if defocus/stigmator measures are applied and compared for images of the same sample obtained with different microscope settings.

The alternative approach to extracting power spectrum parameters could be simply fitting it with a continuous model [4] by minimizing least square difference of continuous and experimental data with the help of an iterative method (for instance, Newton method). In [4] this is done for one-dimensional case under the assumption that power spectrum is rotationally symmetric. For one-dimensional case this would take much longer computational time than computing of defocus/stigmator functions, which is non-iterative.

Another approach for extracting defocus/stigmator information from power spectrum could be based on a non-iterative fitting of discrete power spectrum with a set of basis functions, for instance, via projection method [23]. In this case the defocus/stigmator function could be pre-computed analytically for the given set of basis functions. However, for the set of basis function explored so far, the approach is still slower than direct computation of focus/stigmatic function described in this paper.

Acknowledgment

We would like to thank Seyno Sluyterman (FEI, the Netherland) for ideas, support, thoughtful discussions and processing the results. We are thankful to Max Otten, Rob van Vucht (FEI, the Netherland) Dirk Van Dyck, Wouter van den Broek (EMAT, Belgium) for thoughtful discussions. We kindly acknowledge Rob van Vucht and Michael Janus (FEI, the Netherland) for assistance with obtaining the experimental data.

This work has been carried out as a part of the Condor project at FEI Company under

the responsibilities of the Embedded Systems Institute (ESI). This project is partially supported by the Dutch Ministry of Economic Affairs under the BSIK program.

References

[1] M. Abramowitz and I.A. Stegun. *Handbook on mathematical functions with formulas, graphs, and mathematical tables*, chapter Modified Bessel functions, pages 374–377. Dover, New York, 9th printing edition, 1972.

[2] N. Baba, K. Terayama, T. Yoshimizu, N. Ichise, and N. Tanaka. An auto-tuning method for focusing and astigmatism correction in HAADF-STEM, based on the image contrast transfer function. *Ultramicroscopy*, 50:163–176, 2001.

[3] A.S. Carasso. The APEX method in image sharpening and the use of low exponent levy stable laws. *SIAM J. Appl. Math*, 63(2):593–618, 2002.

[4] A.S. Carasso, D.S. Bright, and A.E. Vladar. APEX method and real-time blind deconvolution of scanning electron microscopy imagery. *Opt. Eng*, 41(10):2499–2514, 2002.

[5] S.J. Erasmus and K.C.A. Smith. An automatic focusing and astigmatism correction system for the SEM and CTEM. *J. Microsc.*, 127(2):185–199, 1982.

[6] R.C. Gonzalez, R.E. Woods, and S.L. Eddings. *Digital image processing using MATLAB*. Upper Saddle River: Pearson Prentice Hall, 2004.

[7] M. Haider, H. Muller, and S Uhlemann. *Advances in imaging and electron physics*, volume 153, chapter Present and Future Hexapole Aberration Correctors for High-Resolution Electron Microscopy, pages 43–120. Academic press, Amsterdam, The Netherlands, 2008.

[8] S. Jutamulia, T. Asakura, R.D. Bahuguna, and C. De Guzman. Autofocusing based on power-spectra analysis. *Applied optics*, 33(26):6210–6212, 1994.

[9] E.J. Kirkland. *Advanced Computing in Electron Microscopy*. Plenum Press, 1998.

[10] O.L. Krivanek and P.E. Mooney. Applications of slow-scan CCD cameras in transmission electron microscopy. *Ultramicroscopy*, 49:95–108, 1993.

[11] E. Krotkov. Focusing. *Int. J. Comput. Vis.*, 1:223–237, 1987.

[12] X.Y. Liu, W.H. Wang, and Y. Sun. Dynamic evaluation of autofocusing for automated microscopic analysis of blood smear and pap smear. *J. Microsc.*, 227:15–23, 2007.

[13] S. Mallat. *A Wavelet Tour of Signal Processing*. Academic Press, 2nd ed. edition, 1999.

[14] K. Nakamae, M. Chikahisa, and Fujioka H. Estimation of electron probe profile from sem image through wavelet multiresolution analysis for inline sem inspection. *Image. Vis. Comp.*, 25:1117–1123, 2007.

[15] S. K. Nayar and Y. Nakagawa. Shape from focus. *IEEE Trans. Pattern Anal. Mach. Intell.*, 16(8):824–831, 1994.

[16] P.D. Nellist and S.J. Pennycook. Incoherent imaging using dynamically scattered coherent electrons. *Ultramicroscopy*, 78:111–124, 1999.

[17] K.H. Ong, J.C.H. Phang, and J.T.L. Thong. A robust focusing and astigmatism correction method for the scanning electron microscope. *Scanning*, 19:553–563, june 1997.

[18] M.T. Postek and A.E. Vladar. Image sharpness measurement in scanning electron microscopy-Part I. *Scanning*, 20:1–9, 1998.

[19] W.D. Riecke. *Topics in Current Physics: Magnetic Electron Lenses*, chapter Practical lens design, pages 164–351. Spring-Verlag, 1982.

[20] M.E. Rudnaya, S.C. Kho, R.M.M. Mattheij, and J.M.L. Maubach. Derivative-free optimization for autofocus and astigmatism correction in electron microscopy. In *Proc. 2nd International Conference on Engineering Optimization*, Lisbon, Portugal, 2010.

[21] M.E. Rudnaya, R.M.M. Mattheij, and J.M.L. Maubach. Iterative autofocus algorithms for scanning electron microscopy. *Microsc. Microanal.*, 15(Suppl 2):1108–1109, 2009.

[22] M.E. Rudnaya, R.M.M. Mattheij, and J.M.L. Maubach. Evaluating sharpness functions for automated scanning electron microscopy. *J. Microsc.*, 240:38–49, 2010.

[23] M.E. Rudnaya, J.M.L. Maubach, and R.M.M. Mattheij. Scanning electron microscopy: Power spectrum analysis. In *Proc. of 9th Multinational Conference on Microscopy*, pages 185–186, Graz, Austria, 2009.

[24] M.E. Rudnaya, W. Van den Broek, R.M.P. Doornbos, R.M.M. Mattheij, and J.M.L. Maubach. Autofocus and two-fold astigmatism correction in HAADF-STEM. Casa-report 10-09, Eindhoven University of Technology, 2010. http://www.win.tue.nl/analysis/reports/rana10-09.pdf.

[25] A. Santos, C.O. De Solórzano, J.J. Vaquero, J.M. Peña, N. Malpica, and F. Del Pozo. Evaluation of autofocus functions in molecular cytogenetic analysis. *J. Microsc.*, 188:264–272, 1997.

[26] A. Tejada, W. Van Den Broek, S. van der Hoeven, and A.J. den Dekker. Towards STEM control: Modeling framework and development of a sensor for defocus control. In *Proc. 48th IEEE Conference on Decision and Control*, pages 8310–8315, 2009.

[27] G. Tzimiropoulos, N. Mitianoudis, and T. Stathaki. A unifying approach to moment-based shape orientation and symmetry classification. *IEEE Trans. Image Proc.*, 18(1):125–139, 2009.

[28] W.E. Vanderlinde and J.N. Caron. Blind deconvolution of SEM images. In *Proc. 33rd International Symposium for Testing and Failure Analysis*, 2007.

[29] A.E. Vladar, M.T. Postek, and M.P. Davidson. Image sharpness measurement in scanning electron microscopy-Part II. *Scanning*, 20:24–34, june 1998.

[30] T.T.E. Yeo, S.H. Ong, Jayasooriah, and R. Sinniah. Autofocusing for tissue microscopy. *Image Vis. Comput.*, 11(10):629–639, december 1993.

[31] J. Zach and M. Haider. Correction of spherical and chromatic aberration in a low-voltage sem. *Optik*, 98:112–118, 1995.

[32] F. Zemlin, Weiss K., Schiske W., Kunath W., and K.H. Herrmann. Coma-free alignment of high resolution electron microscopes with the aid of optical diffractograms. *Ultramicroscopy*, 3:49–60, 1978.

[33] Y. Zhang, Y. Zhang, and W. Changyun. A new focus measure method using moments. *Image Vis. Comp.*, 18:959–965, 2000.

[34] J. Zunic, P.L. Rosin, and L. Kopanja. On the orientability of shapes. *IEEE Trans. Image Proc.*, 15(11):3478 –3487, 2006.

PREVIOUS PUBLICATIONS IN THIS SERIES:

Number	Author(s)	Title	Month
10-67	A. Hlod J.M.L. Maubach	On error estimation in the fourier modal method for diffractive gratings	Oct. '10
10-68	J.H.M. Evers A. Muntean	Modeling micro-macro pedestrian counterflow in heterogeneous domains	Nov. '10
10-69	S.W. Rienstra M. Darau	Boundary layer thickness effects of the hydrodynamic instability along an impedance wall	Nov. '10
10-70	T. Fatima A. Muntean	Sulfate attack in sewer pipes: Derivation of a concrete corrosion model via two-scale convergence	Nov. '10
10-71	M.E. Rudnaya R.M.M. Mattheij J.M.L. Maubach	Orientation identification of the power spectrum	Dec. '10

Ontwerp: de Tantes,
Tobias Baanders, CWI